Monthly Notices
of the
ROYAL ASTRONOMICAL SOCIETY

MNRAS **428,** 1755–1765 (2013) doi:10.1093/mnras/sts156

Prospects for detecting the 21 cm forest from the diffuse intergalactic medium with LOFAR

B. Ciardi,[1] P. Labropoulos,[2] A. Maselli,[3] R. Thomas,[4] S. Zaroubi,[5]★ L. Graziani,[1] J. S. Bolton,[6] G. Bernardi,[7] M. Brentjens,[2] A. G. de Bruyn,[2,5] S. Daiboo,[5] G. J. A. Harker,[8] V. Jelic,[2] S. Kazemi,[5] L. V. E. Koopmans,[5] O. Martinez,[5] G. Mellema,[9] A. R. Offringa,[5] V. N. Pandey,[2,5] J. Schaye,[10] V. Veligatla,[5] H. Vedantham[5] and S. Yatawatta[2,4]

[1]*Max-Planck-Institut fuer Astrophysik, Karl-Schwarzschild-Strasse 1, D-85748 Garching b. Muenchen, Germany*
[2]*ASTRON, PO Box 2, NL-7990 AA Dwingeloo, the Netherlands*
[3]*EVENT Lab for Neuroscience and Technology, Universitat de Barcelona, Passeig de la Vall d'Hebron 171, E-08035 Barcelona, Spain*
[4]*CITA, University of Toronto, 60 St George Street, Toronto, ON M5S 3H8, Canada*
[5]*Kapteyn Astronomical Institute, University of Groningen, PO Box 800, NL-9700 AV Groningen, the Netherlands*
[6]*School of Physics, University of Melbourne, Parkville, Victoria 3010, Australia*
[7]*Harvard–Smithsonian Center for Astrophysics, 60 Garden Street, Cambridge, MA 02138, USA*
[8]*Center for Astrophysics and Space Astronomy, University of Colorado Boulder, CO 80309, USA*
[9]*Department of Astronomy and Oskar Klein Centre for Cosmoparticle Physics, AlbaNova, Stockholm University, SE-106 91 Stockholm, Sweden*
[10]*Leiden Observatory, Leiden University, PO Box 9513, NL-2300RA Leiden, the Netherlands*

Accepted 2012 October 4. Received 2012 September 25; in original form 2012 August 2

ABSTRACT

We discuss the feasibility of the detection of the 21 cm forest in the diffuse intergalactic medium (IGM) with the radio telescope LOFAR. The optical depth to the 21 cm line has been derived using simulations of reionization which include detailed radiative transfer of ionizing photons. We find that the spectra from reionization models with similar total comoving hydrogen ionizing emissivity but different frequency distribution look remarkably similar. Thus, unless the reionization histories are very different from each other (e.g. a predominance of UV versus X-ray heating) we do not expect to distinguish them by means of observations of the 21 cm forest. Because the presence of a strong X-ray background would make the detection of the 21 cm line absorption impossible, the lack of absorption could be used as a probe of the presence/intensity of the X-ray background and the thermal history of the Universe. Along a random line of sight LOFAR could detect a global suppression of the spectrum from $z \gtrsim 12$, when the IGM is still mostly neutral and cold, in contrast with the more well-defined, albeit broad, absorption features visible at lower redshift. Sharp, strong absorption features associated with rare, high-density pockets of gas could also be detected at $z \sim 7$ along preferential lines of sight.

Key words: intergalactic medium – dark ages, reionization, first stars – radio astronomy – radio continuum: general – radio lines: general.

1 INTRODUCTION

The hyperfine transition of the ground state of the neutral hydrogen atom, $^2S_{1/2}$, is the most direct probe of the content and distribution of neutral hydrogen in the Universe. Recent advances in the construction and planning of powerful radio interferometers (e.g. LOFAR,[1] MWA,[2] SKA[3]) are promising the opportunity to make direct observations of the high-redshift intergalactic medium (IGM), at $z \gtrsim 6.5$.

The attention dedicated to 21 cm studies in cosmology so far has been mainly focused on 21 cm tomography, which would ideally provide a 3D mapping of the evolution of neutral hydrogen

★ E-mail: saleem@astro.rug.nl

[1] http://lofar.org
[2] http://www.mwatelescope.org
[3] http://www.skatelescope.org

(e.g. Madau, Meiksin & Rees 1997; Tozzi et al. 2000; Ciardi & Madau 2003; Mellema et al. 2006; Datta et al. 2008; Lidz et al. 2008; Santos et al. 2008, 2010; Baek et al. 2009; Geil & Wyithe 2009; Morales & Wyithe 2010). Although this is an extremely exciting prospect, it suffers from several severe difficulties (e.g. Shaver et al. 1999; Di Matteo et al. 2002; Di Matteo, Ciardi & Miniati 2004; Geil et al. 2008; Gleser, Nusser & Benson 2008; Jelić et al. 2008; Bernardi et al. 2009, 2010; Bowman, Morales & Hewitt 2009; Liu et al. 2009), the most relevant being foreground and ionospheric contamination, terrestrial interference, low spatial resolution and the requirement that the IGM spin temperature, $T_{\rm s}$, is decoupled from the temperature of the cosmic microwave background (CMB), $T_{\rm CMB}$.

A valid alternative to tomography is looking at the 21 cm lines generated in absorption against high-z radio loud sources by the neutral IGM and intervening collapsed structures, i.e. to search for the 21 cm forest (e.g. Carilli, Gnedin & Owen 2002; Furlanetto & Loeb 2002; Furlanetto 2006; Carilli et al. 2007; Xu et al. 2009; Mack & Wyithe 2012; Meiksin 2011; Xu, Ferrara & Chen 2011). Analogous to the extensively studied case of the Lyα forest (for a review see Meiksin 2009), the 21 cm forest signal can be detected in the spectra of high-z radio sources and results from the absorption produced by the intervening neutral hydrogen along the line of sight (LOS), which removes from the spectrum the continuous radiation locally redshifted to the resonance frequency.

Despite the great challenge posed by the requirement of sufficiently bright, and hence extremely rare, target sources (e.g. Carilli et al. 2002; Xu et al. 2009; Mack & Wyithe 2012), the 21 cm forest is particularly appealing as it naturally bypasses the main limitations expected for 21 cm tomographic measurements. Using 21 cm forest observations provides several benefits: (i) the IGM is visible even if $T_{\rm s} = T_{\rm CMB}$, because the CMB does not act as a background source; (ii) the IGM can be spatially resolved on small scales, of the order of a few tens of kpc or even lower; (iii) spectroscopy of bright point sources is technically easier than 2D image processing, and all problems associated with foregrounds and interference vanish (see Furlanetto 2006, for a more detailed discussion). A further advantage is the close similarity with the Lyα forest, from which one can adopt the well-established and robust analysis techniques described in the literature.

In this paper we discuss the possibility of detecting the 21 cm signal with the radio telescope LOFAR, by making use of the simulations of reionization presented in Ciardi et al. (2012, hereafter C2012). Differently from previous studies mentioned above, the simulations used here are run using a combination of hydrodynamic simulations and the detailed radiative transfer of ionizing photons through a gas composed of hydrogen and helium. The latter component is particularly important for a correct determination of the gas temperature. In addition, the expected observed spectrum is calculated based on the actual LOFAR configuration. In Section 2 we briefly review the basic physics relevant for the 21 cm forest signal. In Section 3 we discuss the adopted simulations, while in Section 4 the method for producing mock spectra of high-z radio loud sources, as well as the dependence on a number of quantities, is presented. In Section 5 we discuss the observational feasibility and in Section 6 we give our conclusions.

2 THE 21 CM FOREST

As the physics behind the emission/absorption of the 21 cm line has been extensively discussed in the literature by several authors (for a review see e.g. Furlanetto, Oh & Briggs 2006), here we just write the relevant equations without derivation. The 21 cm line corresponds to the hyperfine, spin-flip transition of the ground state of the neutral hydrogen atom, $^2{\rm S}_{1/2}$, and to a rest-frame frequency $\nu_{21{\rm cm}} = 1.42$ GHz. A photon travelling through a patch of neutral hydrogen at redshift z will see the optical depth (e.g. Madau et al. 1997; Furlanetto et al. 2006):

$$\tau_{21{\rm cm}}(z) = \frac{3}{32\pi}\frac{h_{\rm p}c^3A_{21{\rm cm}}}{k_{\rm B}\nu_{21{\rm cm}}^2}\frac{x_{\rm HI}n_{\rm H}}{T_{\rm s}(1+z)({\rm d}v_\parallel/{\rm d}r_\parallel)} = 9.6\times10^{-3}x_{\rm HI}(1+\delta)\left(\frac{1+z}{10}\right)^{3/2} \times\left(\frac{T_{\rm CMB}(z)}{T_{\rm s}(z)}\right)\left[\frac{H(z)/(1+z)}{{\rm d}v_\parallel/{\rm d}r_\parallel}\right], \quad (1)$$

where $n_{\rm H}$ is the H number density, δ is the gas density contrast, $x_{\rm HI}$ is the mean neutral hydrogen fraction, $T_{\rm CMB}$ is the CMB temperature, $T_{\rm s}$ is the gas spin temperature (which quantifies the relative population of the two levels of the $^2{\rm S}_{1/2}$ transition), $A_{21{\rm cm}} = 2.85\times10^{-15}$ s^{-1} is the Einstein coefficient of the transition, H is the Hubble parameter and ${\rm d}v_\parallel/{\rm d}r_\parallel$ is the gradient of the proper velocity along the LOS (in km s^{-1}), which takes into account also the contribution of the gas peculiar velocity. The other symbols appearing in the equation above have the standard meaning adopted in the literature. It should be noted that here we do not perform a convolution with a Doppler line profile. Although we do not expect this approximation to affect our estimates of the detectability of absorption lines with LOFAR, we are planning to investigate this issue in more detail in the future.

The photons emitted by a radio loud source at redshift $z_{\rm s}$ with frequencies $\nu > \nu_{21{\rm cm}}$ will be removed from the source spectrum with a probability $(1-{\rm e}^{-\tau_{21{\rm cm}}})$, absorbed by the neutral hydrogen present along the LOS at redshift $z = (\nu_{21{\rm cm}}/\nu)(1+z_{\rm s})-1$. Analogously to the case of the Lyα forest, this could result in an average suppression of the source flux (produced by diffuse neutral hydrogen), as well as in a series of isolated absorption lines (produced by overdense clumps of neutral hydrogen).

Due to the several orders of magnitude difference in the corresponding Einstein coefficients, the physical regimes in which the 21 cm forest and the Lyα forest are relevant are significantly different. As a consequence of the extremely low value of $A_{21{\rm cm}}$, the 21 cm absorption is not saturated at high redshifts, as is the case for the Lyα forest. This makes the 21 cm forest signal suitable for studying the IGM in the epoch prior to reionization, complementarily to the Lyα forest which instead is more appropriate for post-reionization studies. Nevertheless, the 21 cm forest detection is in practice extremely hard, mainly due to the tremendously weak 21 cm magnetic hyperfine transition. As can be easily inferred from equation (1), the associated optical depth is above 0.1, and could therefore produce an observable signal, only under severe physical conditions (i.e. highly neutral, dense and cold gas). Considering furthermore the paucity of radio loud sources at the high redshifts of interest, and their anti-correlation with the optical depth due to the fact that these kinds of objects are thought to be associated with large ionizing fluxes, it is immediately clear that the detection of a 21 cm forest signal is an extremely challenging experiment.

3 SIMULATIONS OF REIONIZATION

The modelling of mock spectra has been done in two main steps. As can be seen from equation (1), the optical depth and thus the absorption along the LOS to a high-redshift source depends significantly on the gas spin temperature, as well as on the neutral

hydrogen fraction at each point along the LOS. The evolution of both these quantities and their spatial fluctuations is determined by the complex process of reionization, which needs to be properly modelled. The first step in our spectra modelling pipeline, which is described below, is then to simulate realistic reionization scenarios. The second step is to use the outputs of such simulations to extract random LOS and build mock absorption spectra of sources at different redshifts. More details are given below in Section 4. Unless stated otherwise, we assume that the spin temperature is coupled to the gas temperature, T.

The simulations we use are described in C2012. Here we just give some basic information and we refer the reader to the original paper for more details.

The simulations are based on a combination of hydrodynamic simulations performed using the parallel Tree-SPH code GADGET-3 (which is an updated version of the publicly available code GADGET-2; see Springel 2005) and of 3D radiative transfer of both H and He followed by the Monte Carlo code CRASH (Ciardi et al. 2001; Maselli, Ferrara & Ciardi 2003; Maselli, Ciardi & Kanekar 2009; Pierleoni, Maselli & Ciardi 2009; Partl et al. 2011; Graziani et al. in preparation). The hydrodynamic simulations were run in boxes of comoving size 35.12 h^{-1} Mpc, with cosmological parameters $\Omega_\Lambda = 0.74$, $\Omega_\mathrm{m} = 0.26$, $\Omega_\mathrm{b} = 0.024\,h^{-2}$, $h = 0.72$, $n_\mathrm{s} = 0.95$ and $\sigma_8 = 0.85$, where the symbols have the usual meanings. A total of 2×512^3 dark matter and gas particles were followed in the simulation, yielding a mass per gas particle of $4.15 \times 10^6\,h^{-1}$ M$\odot$. After the simulation outputs were obtained, the gas densities, peculiar velocities, temperatures and halo masses were interpolated on to a uniform 128^3 grid for the radiative transfer calculations. The emissivity and spectra of the sources were chosen based on a semi-analytic model which satisfies a number of observational constraints, among them the Thomson scattering optical depth and the H I photoionization rate measured from the Lyα forest. The spectra adopted are always power laws, with index = 1, 1.8 or 3. Our reference run ($\mathcal{E}$1.2-α3 in the original paper) has $\alpha = 3$. In Fig. 1 maps of the temperature (left-hand panels) and neutral fraction (right-hand panels) are shown at redshifts $z = 14$, 9 and 7, which correspond to volume-averaged H II fractions $x_{\mathrm{H\,II}}$ (gas temperature T) of 0.029, 0.481 and 0.852 (488, 6020 and 10 643 K), respectively. This simulation mimics a late reionization model, while the other three simulations have been run with a higher comoving hydrogen ionizing emissivity (see equation 3 of C2012) and reach full reionization at an earlier time. These all have a similar emissivity assuming that 30 per cent (70 per cent) of the sources have $\alpha = 1$ (3) (model $\mathcal{E}$1.2-α1-3), or that all sources have $\alpha = 3$ (model $\mathcal{E}$1.6-α3) or $\alpha = 1.8$ (model $\mathcal{E}$1.2-α1.8). The characteristics of the models are summarized in table 1 of C2012. As mentioned, with the exception of $\mathcal{E}$1.2-α3 all the simulations have similar comoving hydrogen ionizing emissivities, so any differences in the reionization histories are only due to the different spectral energy distributions. The evolution of $x_{\mathrm{H\,II}}$ is very similar in all models by construction, while He II reionization is completed progressively later in models $\mathcal{E}$1.6-α3 and $\mathcal{E}$1.2-α3, which have softer ionizing spectra. For more details on the results we refer the reader to C2012.

It should be noticed that the outputs of the simulations are sufficiently close to each other in redshift space that there is always some overlap in the redshift range spanned by subsequent boxes. In particular, we will be using boxes B_i (with $i = 1, \ldots, 54$) which span the redshift range $z \approx 6{-}15$.

While the above simulations are useful to investigate the effect of different reionization histories on the observability of the 21 cm

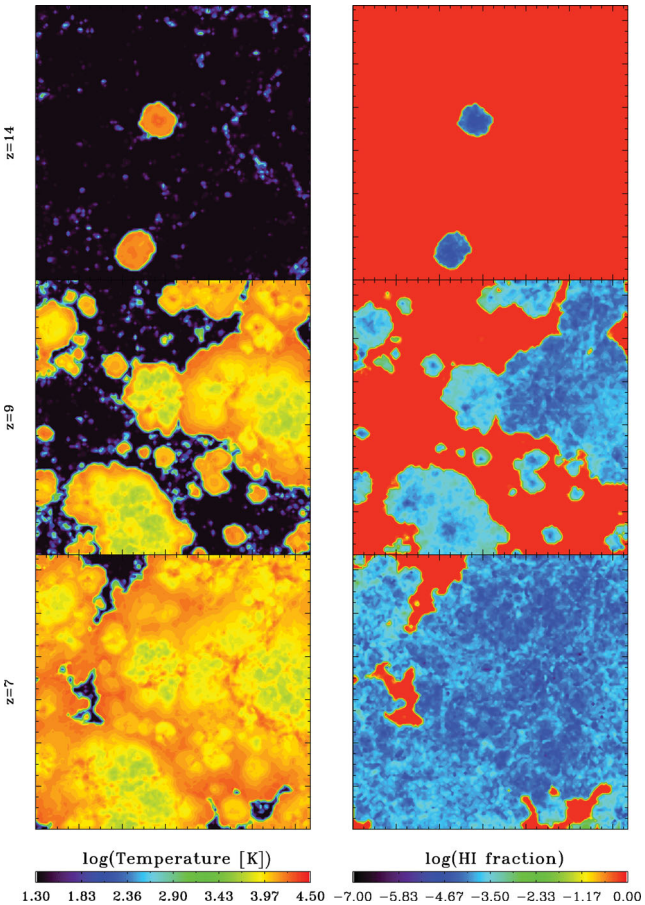

Figure 1. Left-hand panel: maps of temperature at redshift $z = 14$ (upper panel), 9 (central panel) and 7 (lower panel) for the simulation $\mathcal{E}$1.2-α3. Each map represents the central slice of the simulation box. Right-hand panel: as the left-hand panel but for the H II fraction.

absorption features, we have run an additional, higher resolution simulation in a 4.39 h^{-1} Mpc box with the aim of exploring instead the impact of resolution on our results. This simulation has been run with 2×256^3 gas and dark matter particles, corresponding to a mass of the gas particle of $6.48 \times 10^4\,h^{-1}$ M$\odot$, and thus it is better suited to capture the absorption features due to high-density gas at smaller scales. The simulation is similar to the one analysed and discussed in Jeeson Daniel et al. (in preparation), but here we have chosen an amplitude of the total comoving hydrogen ionizing emissivity $\mathcal{E} = 1.8$ (see equation 3 in C2012) and $\alpha = 3$ (in the remaining we will refer to this simulation as $\mathcal{L}$4.39). These choices were motivated by the requirement that the evolution of the neutral fraction was similar to that of our reference run $\mathcal{E}$1.2-α3. As a reference, simulation $\mathcal{E}$1.2-α3 ($\mathcal{L}$4.39) has $x_{\mathrm{H\,I}}$=0.971 (0.974), 0.519 (0.494) and 0.148 (0.151) at $z = 14$, 9 and 7, respectively. Despite the fact that such a small box is not able to capture the reionization process as a whole, it still matches the available observables as the larger boxes do, and it is more appropriate to investigate resolution effects. Also in this case the outputs of the simulations are sufficiently close to each other in redshift space that there is always some overlap between subsequent boxes. Differently from earlier though, we now have a larger number of boxes B_i (with $i = 1, \ldots, 450$) spanning the same redshift range $z \approx 6$–15.

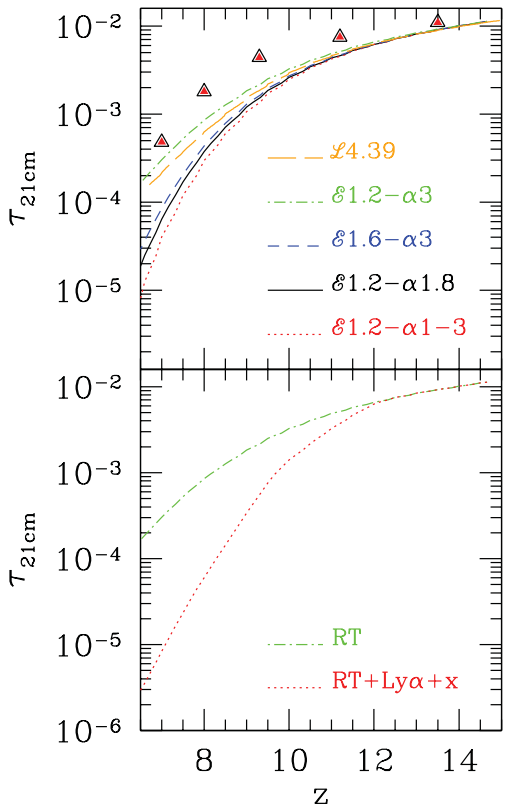

Figure 2. Upper panel: evolution of the volume-averaged 21 cm optical depth for models $\mathcal{E}1.2$-$\alpha1.8$ (black solid line), $\mathcal{E}1.2$-$\alpha1$-3 (red dotted), $\mathcal{E}1.6$-$\alpha3$ (blue dashed), $\mathcal{E}1.2$-$\alpha3$ (green dot–dashed) and $\mathcal{L}4.39$ (orange long-dashed). The triangles refer to the values in the simulation by Xu et al. (2009). Bottom panel: evolution of the volume-averaged 21 cm optical depth in model $\mathcal{E}1.2$-$\alpha3$ for different assumptions about the spin temperature, T_s, being the same as the gas temperature, T, determined from the radiative transfer simulation (green dot–dashed line); the maximum between T and the temperature calculated including also the contribution from Lyα photons from stars and X-ray photons from quasars (red dotted line). See the text for more details.

3.1 Optical depth to the 21 cm line

In the upper panel of Fig. 2 we show the evolution of the volume-averaged (over the entire box) 21 cm optical depth for all models. The value of τ_{21cm} is the same in all models at the highest redshifts, when the evolution of both the H II fraction and temperature is similar (see C2012 for more details). Differences are more evident at lower z. In particular, in model $\mathcal{E}1.2$-$\alpha3$, τ_{21cm} is up to one order of magnitude higher, because reionization is delayed compared to the other cases, for which differences are smaller. More specifically, $\mathcal{E}1.6$-$\alpha3$ has a similar x_{Hi}, but lower temperature compared to $\mathcal{E}1.2$-$\alpha1.8$ and $\mathcal{E}1.2$-$\alpha1$-3, resulting in a slightly higher value of the optical depth. On the other hand, these latter two models have very similar values for both x_{Hi} and T, and the differences in the volume-averaged optical depth arise from more subtle details of the distribution of the physical quantities. As mentioned above, the reionization history in run $\mathcal{L}4.39$ is very similar to that of $\mathcal{E}1.2$-$\alpha3$, with a slightly (few per cent) lower value of x_{Hi} and a slightly (few per cent) larger value of the volume-averaged temperature.[4] The above results in a lower τ_{21cm}.

In the lower panel of Fig. 2 we show the evolution of the volume-averaged 21 cm optical depth in model $\mathcal{E}1.2$-$\alpha3$ for different assumptions about the spin temperature, T_s. The green dot–dashed line is our reference case, in which T_s is assumed to be in equilibrium with the gas temperature, T, calculated from the radiative transfer simulation (which includes only UV photons). The same result is obtained when T_s is calculated as the maximum between the gas temperature as determined from the radiative transfer calculation and that including also the contribution from Lyα photons from stars. If in addition to the Lyα photons we also consider the contribution from X-ray photons from quasars (red dotted line), the gas temperature increases and as a consequence the optical depth decreases. The temperature with Lyα and X-ray photons is calculated for a gas at the mean density using the semi-analytic approach as described in Ciardi, Salvaterra & Di Matteo (2010). Here, the authors calculate the photon production from a population of stars and micro-quasars in a set of cosmological hydrodynamic simulations (Pelupessy, Di Matteo & Ciardi 2007) which self-consistently follow the dark matter dynamics, radiative processes as well as star formation, black hole growth and associated feedback processes. We refer the reader to the original papers for more details. More specifically, the gas temperature as determined by Lyα photons from stars is given by the short-dash–dotted blue line in fig. 2 of that paper, while the one with also heating from X-rays from quasars corresponds to the solid black line in the same plot. While in cells which have been (also partially) ionized the temperature is $\sim10^4$ K, cells which have not been reached by ionizing photons have a temperature which can be as cold as that of the CMB. In this case, a contribution to the heating from Lyα or X-ray photons can raise the temperature above its original value, reducing the optical depth to 21 cm. It should be noted that the above results depend on the model adopted for the Lyα and X-ray photon production, and that this is not self-consistent with the radiative transfer (RT) calculations. While we will address this point more thoroughly in future developments by running radiative transfer simulations which follow self-consistently also the propagation of X-ray and Lyα photons, the qualitative results will still hold.

As a reference, the τ_{21cm} calculated in model $\mathcal{E}1.2$-$\alpha3$ is $\sim$16 per cent (50 per cent) lower than the one found by Xu et al. (2009) at $z = 13.5$ (9.3), and it becomes $\sim$100 per cent larger at $z = 6$. These values are lower than those found by Mack & Wyithe (2012) in their model without X-ray heating, most probably because they obtain an average gas temperature which is never above $\sim$1000 K (also when X-ray heating is included) in the relevant redshift range, i.e. about one order of magnitude lower than the one found in our models.

It should be noted that in all cases τ_{21cm} is just an average value, but the scatter is very large, as can be seen in Fig. 3, where the distribution of 21 cm optical depth versus gas number density is shown for two reference simulations at redshifts $z = 14$ (top panels), 9 (middle panels) and 7 (lower panels). In the 35 h^{-1} Mpc box, most of the gas is initially concentrated either in high-density and high-optical-depth cells (corresponding to cold, neutral, high-density regions) or in cells with $\tau_{21cm} \sim 10^{-9}$ (corresponding to the gas which has been ionized and heated to high temperatures). As reionization proceeds and more cells get ionized, the corresponding optical depth decreases. We also observe a larger spread of τ_{21cm} with the gas number density, due to the fact that photons have now reached low-density regions far away from the location of the

[4] Despite having the same mean density of the larger box, the 4.39 h^{-1} box has gas at higher density. Because of this, more ionizing photons are needed to maintain a similar ionization fraction, with the consequence of an increased photo-heating.

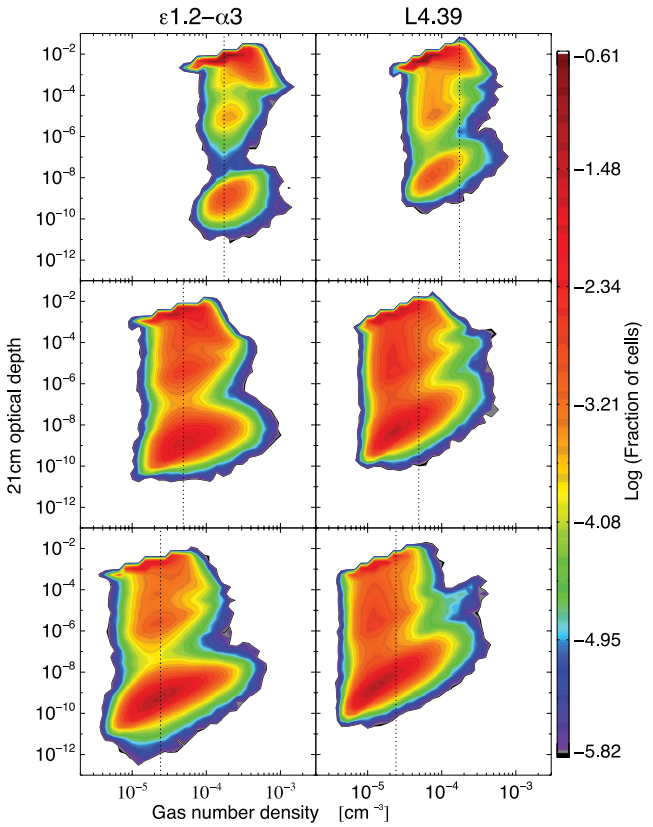

Figure 3. Distribution of the 21 cm optical depth versus gas number density for models $\mathcal{E}1.2$-$\alpha3$ (left-hand panel) and $\mathcal{L}4.39$ (right-hand panel). The rows refer to redshifts $z = 14$, 9 and 7 (from top to bottom). The vertical lines refer to the volume-averaged gas number density in the box, which corresponds to $\delta = 1$.

sources of radiation. While at $z = 9$ there is still a large range of values of the optical depth, at $z = 7$ most cells have $\tau_{21\rm cm} \sim 10^{-10}$, because reionization is almost complete. It is interesting to compare the distribution of the optical depth to the one of the gas temperature shown in fig. 7 of C2012. In fact, the two quantities exhibit a complementary behaviour, as expected. The distribution and evolution of $\tau_{21\rm cm}$ for $\mathcal{L}4.39$ are similar, although the optical depth is always higher, and the range of densities spanned is larger compared to the other models.

A more quantitative representation is given in Fig. 4, where we show the percentage of cells as a function of the transmissivity, $\exp(-\tau_{21\rm cm})$, i.e. the quantity most relevant to observations (see the following section). In all models, at the highest redshift most of the cells have a high optical depth (i.e. $\exp(-\tau_{21\rm cm}) < 1$), although, as already mentioned, there is a large spread and the cells which have already been ionized are concentrated around $\tau_{21\rm cm} \sim 10^{-9}$ (i.e. $\exp(-\tau_{21\rm cm}) \sim 1$). As ionization proceeds, the number of cells with such optical depth increases, while those with higher $\tau_{21\rm cm}$ decreases. This results in a shift towards larger values of the transmissivity. At all redshifts there are also intermediate values of $\tau_{21\rm cm}$, reflecting the distribution of densities and temperatures (see C2012). The limitations due to resolution effects are visible at all redshifts as a sudden drop of the number of cells below a minimum transmissivity. The behaviour is very similar in all models, with a systematically lower transmissivity for $\mathcal{L}4.39$. Due to the higher resolution of $\mathcal{L}4.39$, larger values for the gas overdensity are sampled in this simulation. It should be noted though that also in this

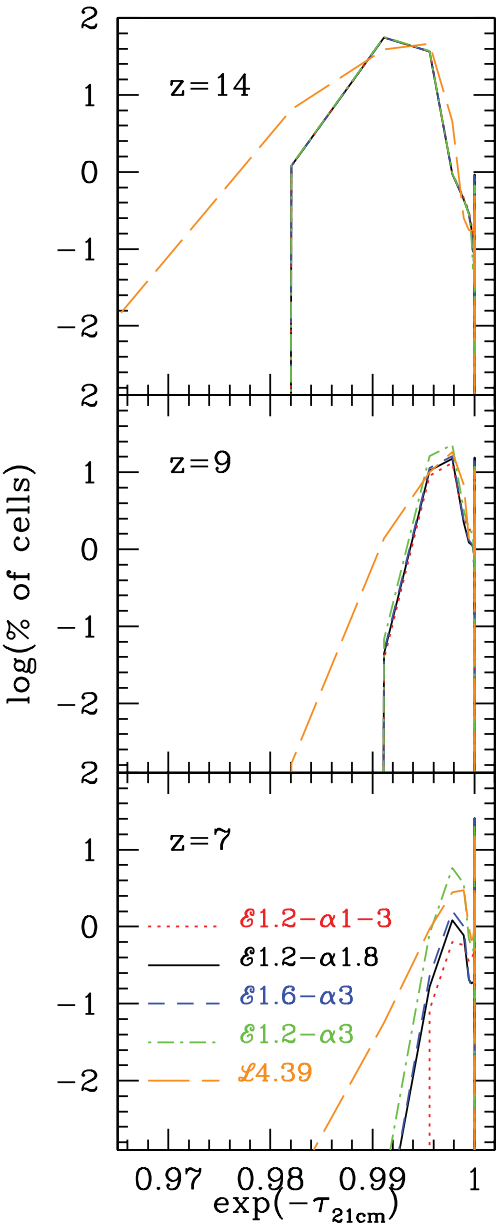

Figure 4. Percentage of cells as a function of the transmissivity, $\exp(-\tau_{21\rm cm})$, at $z = 14$ (upper panel), 9 (middle) and 7 (lower). The black solid, red dotted, blue dashed, green dot–dashed and orange long-dashed lines indicate results for models $\mathcal{E}1.2$-$\alpha1.8$, $\mathcal{E}1.2$-$\alpha1$-3, $\mathcal{E}1.6$-$\alpha3$, $\mathcal{E}1.2$-$\alpha3$ and $\mathcal{L}4.39$, respectively.

smaller simulation the resolution is not enough to capture the even higher overdensities which are associated with collapsed objects. This topic is the focus of a future investigation.

In Fig. 5 the gas overdensity of cells with optical depth larger than $\tau_{21\rm cm}$ is plotted at redshifts $z = 14$, 9 and 7 for models $\mathcal{L}4.39$ and $\mathcal{E}1.2$-$\alpha3$. The shaded areas refer to the full range of overdensities, while the solid lines indicate the mean values. It is evident that, while the mean value is similar in both cases (because the hydrodynamical simulations have the same mean density), $\mathcal{L}4.39$ reaches higher overdensities which produce the larger values of the optical depth. This is important for the observability of the line, as we will see in the following.

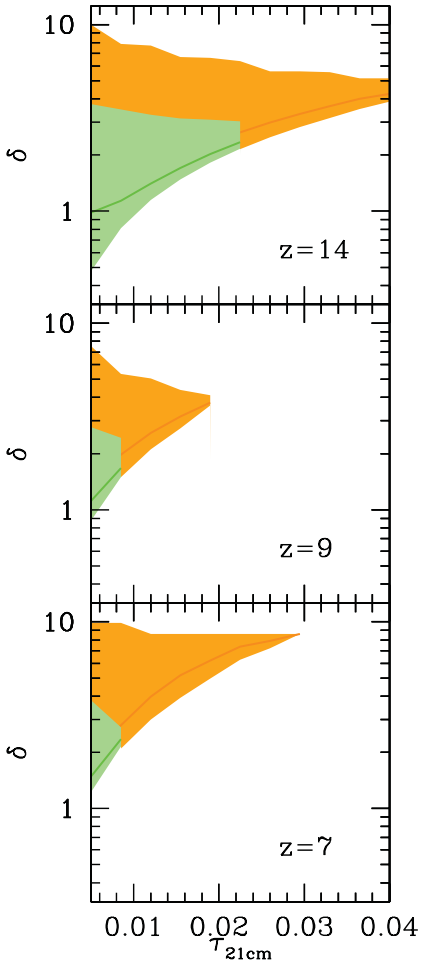

Figure 5. Gas overdensity of cells with optical depth larger than $\tau_{21\mathrm{cm}}$ at redshift $z = 14$ (upper panel), 9 (middle) and 7 (lower) for models $\mathcal{L}4.39$ (orange shaded area in the back) and $\mathcal{E}1.2$-$\alpha 3$ (green shaded area in the front). The shaded areas refer to the full range of overdensities, while the solid lines indicate the mean values.

4 MOCK SPECTRA

From each simulation box B_i we extract 2500 random LOS. A total LOS is obtained as follows. We choose randomly an LOS (los_1) among those built from box B_1 and we stack it with one (los_2) chosen randomly among those built from box B_2. Whenever los_1 and los_2 overlap in redshift, we average the relevant quantities. For example, $n_{\mathrm{H\,I}}(z)$ of the total LOS is given by $[n_{\mathrm{H\,I},i}(z) + n_{\mathrm{H\,I},i+1}(z)]/2$, where $n_{\mathrm{H\,I},i}(z)$ is the H I number density at redshift z in los_i. This procedure is repeated for all the boxes.

An example of such an LOS from model $\mathcal{E}1.2$-$\alpha 3$ is shown in Fig. 6. Here the panels (from top to bottom) indicate the evolution of H number density, H I fraction, gas temperature and transmissivity, $\mathrm{e}^{-\tau_{21\mathrm{cm}}}$. The dotted lines indicate the volume-averaged values of the different quantities. It should be noted that here no smoothing has been applied and the resolution shown corresponds to the one of the simulation, i.e. ∼15–20 kHz depending on redshift. We will discuss the higher resolution simulations in Section 5, while here (Fig. 7) we just show the transmissivity along a random LOS as a comparison with the larger box. Below, we will discuss the dependence of our results on a number of quantities, using the simulations run in the 35 h^{-1} Mpc box.

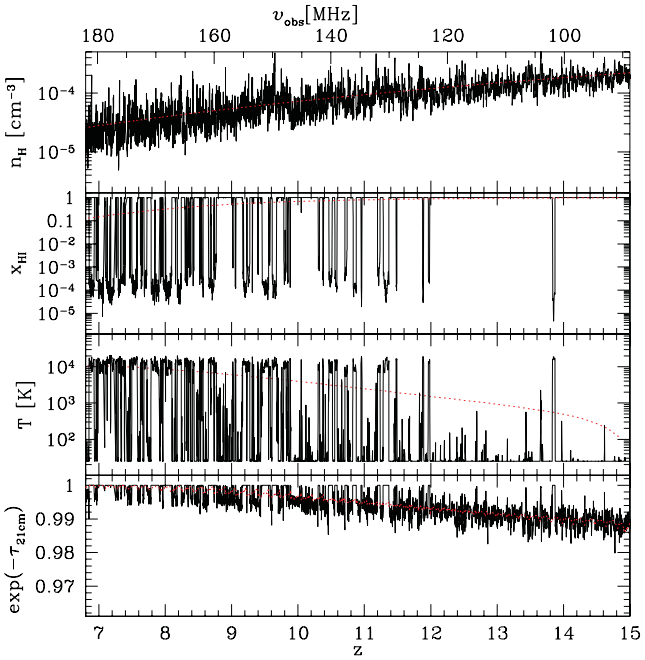

Figure 6. Physical state of the gas along a random LOS (solid lines) in model $\mathcal{E}1.2$-$\alpha 3$. From top to bottom: physical H number density, H I fraction, gas temperature, gas transmissivity. The red dotted lines indicate the volume-averaged values of the different quantities.

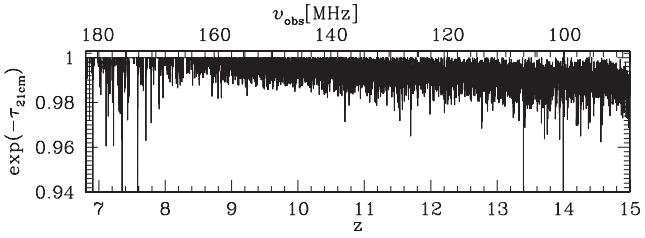

Figure 7. Gas transmissivity along a random LOS in model $\mathcal{L}4.39$.

4.1 Dependence on spin temperature

In Fig. 8 the dependence on different assumptions about the gas spin temperature is shown. The LOS is the same as that plotted in Fig. 6, but now we show not only the reference case (upper panel), but also a case in which T_{s} is taken to be the maximum of the gas temperature as determined from the radiative transfer calculation (which includes only UV photons) and that including also the contribution from Lyα photons from stars (middle panel) and from Lyα plus X-ray photons from quasars (lower panel). More details on the calculation of the temperature are given in Section 3.1. Because Lyα heating is not extremely efficient, the resulting transmissivity is very similar to the case without such heating. In contrast, the contribution from x-rays is more substantial and this can clearly be seen in the figure as a reduction of the transmissivity at redshifts when the extra heating is significant ($z \lesssim 12$). This suggests that in the presence of X-ray heating, the detection of the 21 cm forest would most probably not be feasible (but see e.g. Mack & Wyithe 2012 and Xu et al. 2011 for a discussion of the dependence of absorption features on the strength of the X-ray heating). It should be noted that the value of the X-ray background used here is appropriate for a population of high-z quasars. As a reference, at $z = 10$ it is $\sim 4 \times 10^{-26}$ ergs cm^{-2} s^{-1} Hz^{-1} sr^{-1} (see fig. 1 of Ciardi et al. 2010). If the background were instead dominated by

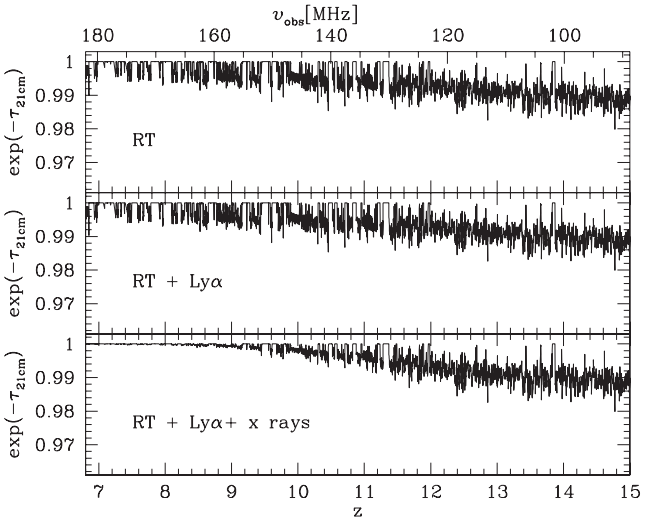

Figure 8. Evolution of the gas transmissivity along a random LOS for different assumptions about the gas temperature, T. From top to bottom the gas temperature is the one determined from the radiative transfer of UV photons only; the maximum of the one determined from the radiative transfer of UV photons and the one calculated including also the contribution from Lyα photons from stars; the maximum of the one determined from the radiative transfer of UV photons and the one calculated including also the contribution from Lyα photons from stars and X-ray photons from quasars.

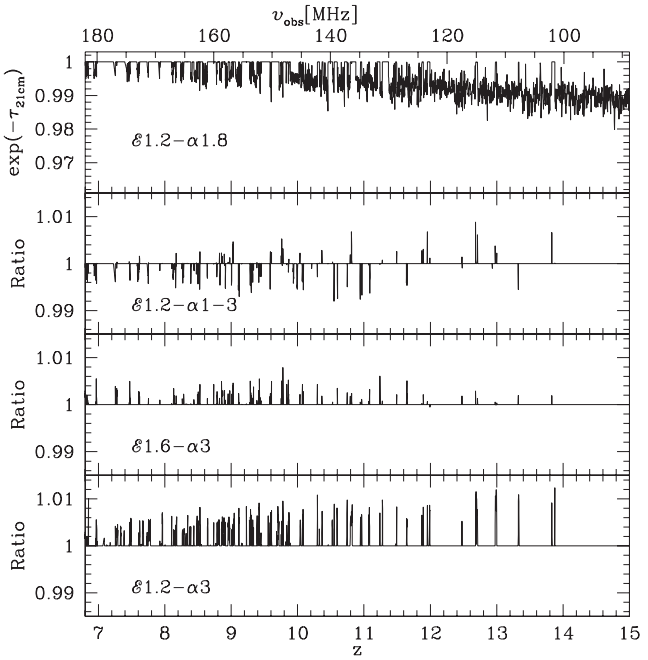

Figure 9. From the top to the bottom panels we show the evolution of the gas transmissivity along a random LOS for the reionization model $\mathcal{E}1.2$-$\alpha1.8$, and the ratios between the transmissivity of model $\mathcal{E}1.2$-$\alpha1.8$ and models $\mathcal{E}1.2$-$\alpha1$-3, $\mathcal{E}1.6$-$\alpha3$ and $\mathcal{E}1.2$-$\alpha3$, respectively. The ratios have been calculated using the same LOS as the upper panel.

a different class of sources, as X-ray binaries (see e.g. Furlanetto 2006; Dijkstra et al. 2012), then the associated heating would be different. We defer to future work a more detailed investigation of the role of the X-ray background and the contribution to it from different types of sources.

As already pointed out by other authors (e.g. Mack & Wyithe 2012), the above arguments seem to suggest that it would be possible to discriminate between different IGM reheating histories, in particular if a high-energy component were present in the ionizing spectrum.

4.2 Dependence on source spectra

As discussed in Section 3, the simulations have been run for a variety of source spectra. Here we show the differences induced in terms of transmission. In the top panel of Fig. 9 a reference LOS for the reionization model $\mathcal{E}1.2$-$\alpha1.8$ is shown. In the other panels the ratios between the transmissivity of model $\mathcal{E}1.2$-$\alpha1.8$ and models $\mathcal{E}1.2$-$\alpha1$-3, $\mathcal{E}1.6$-$\alpha3$ and $\mathcal{E}1.2$-$\alpha3$ are plotted. In the third and fourth panels from the top the ratio is always larger than 1, meaning that the optical depth in $\mathcal{E}1.2$-$\alpha1.8$ is lower than in $\mathcal{E}1.6$-$\alpha3$ and $\mathcal{E}1.2$-$\alpha3$ (i.e. the simulations with softer spectra), as expected. In fact, although $x_{\rm Hi}$ is very similar in $\mathcal{E}1.2$-$\alpha1.8$ and $\mathcal{E}1.6$-$\alpha3$, the temperature in the latter is typically lower, resulting in a higher optical depth. On the other hand, as in model $\mathcal{E}1.2$-$\alpha3$ reionization is less advanced, the optical depth is always larger than for the other cases. Models $\mathcal{E}1.2$-$\alpha1.8$ and $\mathcal{E}1.2$-$\alpha1$-3 have very similar average $x_{\rm Hi}$ and T, but their distributions are slightly different. This reflects also on the transmissivity.

These very small differences in transmissivity predicted by different reionization models are to be expected. As discussed in the previous section, the models do have different values of $\tau_{21\rm cm}$, but these are more pronounced when $\tau_{21\rm cm}$ is in any case too low to produce appreciable absorption. In fact, all models have very similar hydrogen reionization histories, with the largest discrepancies being associated with the temperature reached either in the ionized regions or in their outskirts, where the hardness of the spectrum makes most of the difference. From the point of view of the absorption, though, the exact value of the temperature in a fully or partially ionized cell is not relevant. On the other hand, the regions which produce most of the absorption, i.e. the cold, high-density gas not reached by ionizing photons, are basically the same in all models. Thus, unless the reionization histories are very different from each other (e.g. a predominance of UV versus X-ray sources), we do not expect to be able to distinguish them by means of observations of the 21 cm forest.

5 INSTRUMENTAL EFFECTS

In this section we describe the process used to simulate the spectra as they would be observed by LOFAR. The input of the simulation is a file containing the optical depth as a function of redshift (or, equivalently, frequency) and the parameters associated with the background radio source, i.e. its redshift, $z_{\rm s}$, flux density, $S_{\rm in}(z_{\rm s})$, and spectral index, α. Consistently with previous studies (e.g. Carilli et al. 2002) we assume that the source has a power-law spectrum. In principle, the effect of the point spread function side lobes running through the source of interest can be taken into account by including more sources at different positions, with or without absorption features. Here, this has not been considered. For a narrow bandwidth, the equation giving the observed visibilities is

$$V_\nu(\boldsymbol{u}) = \sum_i^{N_{\rm sources}} I_\nu(\boldsymbol{s}) {\rm e}^{-2\pi i \boldsymbol{u}\cdot\boldsymbol{s}} + n, \quad (2)$$

where $\boldsymbol{u} = (u, v, w)$ are the coordinates of a given baseline at a certain time t, I_ν is the observed source intensity, $\boldsymbol{s} = (l, m, n)$ is a vector representing the direction cosines for a given source direction

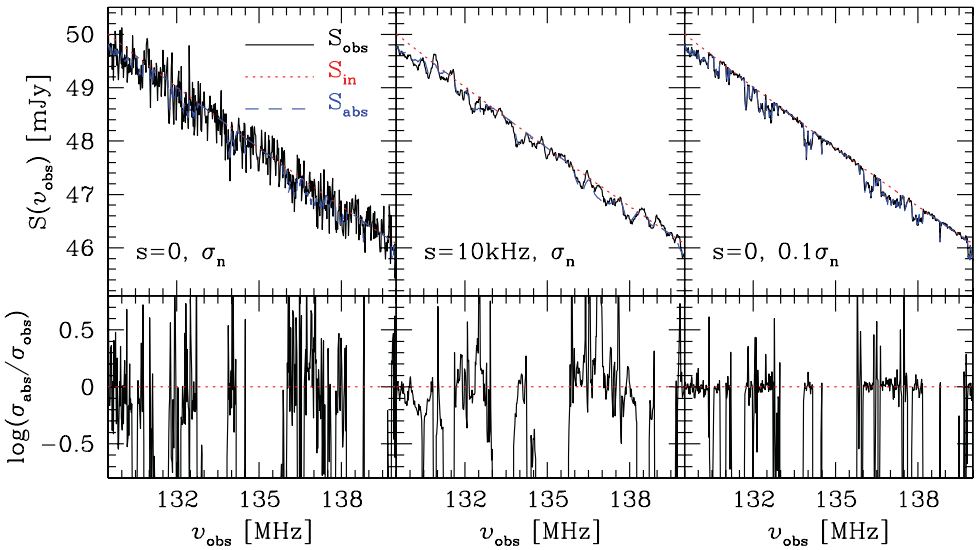

Figure 10. Upper panels: spectrum of a source positioned at $z_s = 10$ (i.e. $\nu \sim 129$ MHz), with a power-law index of $\alpha = 1.05$ and a flux density of $S_{\rm in}(z_s) = 50$ mJy. The red dotted lines refer to the intrinsic spectrum of the radio source, $S_{\rm in}$; the blue dashed lines to the simulated spectrum for 21 cm absorption, $S_{\rm abs}$; and the black solid lines to the spectrum for 21 cm absorption as it would be seen by LOFAR. The latter has been calculated assuming an observation time $t_{\rm int} = 1000$ h and a bandwidth $\Delta\nu = 20$ kHz. The IGM absorption is calculated from the reference simulation $\mathcal{E}1.2$-$\alpha3$. Left-hand panel: $S_{\rm abs}$ and $S_{\rm obs}$ are obtained without smoothing, $s = 0$, and with the noise σ_n given in equation (3). Middle panel: $S_{\rm abs}$ and $S_{\rm obs}$ are obtained after smoothing over a scale $s = 10$ kHz, and with the noise σ_n given in equation (3). Right-hand panel: $S_{\rm abs}$ and $S_{\rm obs}$ are obtained without smoothing, $s = 0$, and with 1/10th of the noise σ_n given in equation (3). Lower panels: $\sigma_{\rm abs}/\sigma_{\rm obs}$ corresponding to the upper panels. Here $\sigma_i = S_i - S_{\rm in}$, with $i =$ abs, obs. See the text for further details.

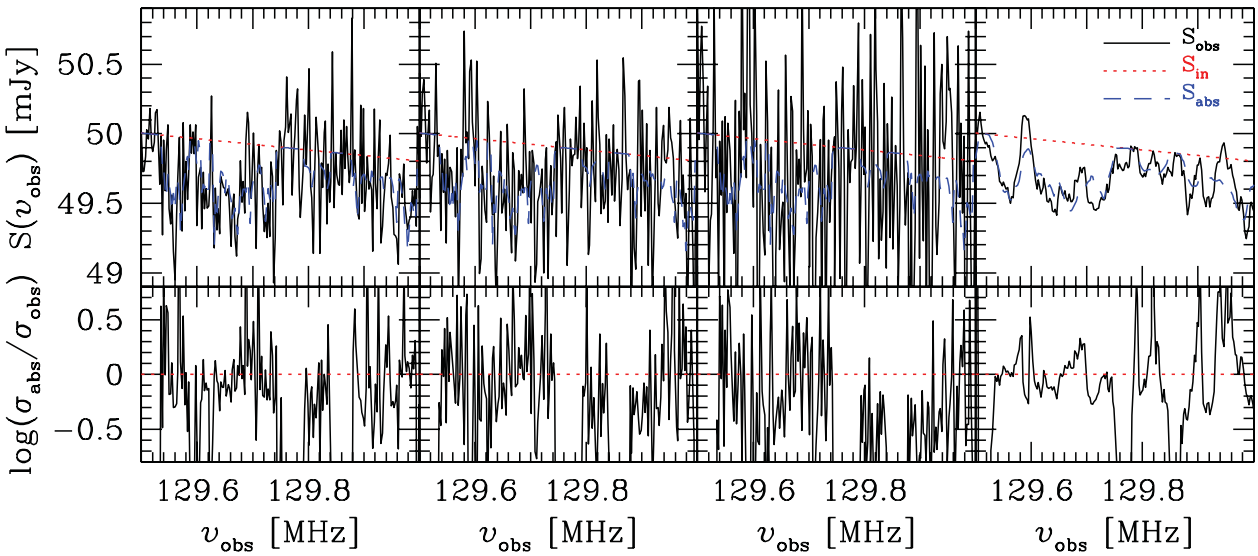

Figure 11. Upper panels: spectrum of a source positioned at $z = 10$ (i.e. $\nu \sim 129$ MHz), with an index of the power law $\alpha = 1.05$ and a flux density $S_{\rm in}(z_s) = 50$ mJy. The lines are the same as those in Fig. 10. $S_{\rm obs}$ has been calculated assuming the noise σ_n given in equation (3). The IGM absorption is calculated from the reference simulation $\mathcal{L}4.39$. From left to right the panels refer to a case in which $S_{\rm abs}$ and $S_{\rm obs}$ are obtained: with a bandwidth $\Delta\nu = 20$ kHz, without smoothing, $s = 0$, and with an integration time $t_{\rm int} = 1000$ h; with a bandwidth $\Delta\nu = 20$ kHz, without smoothing, $s = 0$, and with an integration time $t_{\rm int} = 500$ h; with a bandwidth $\Delta\nu = 2.5$ kHz, smoothing over a scale $s = 2.5$ kHz, and with an integration time $t_{\rm int} = 1000$ h; with a bandwidth $\Delta\nu = 10$ kHz, smoothing over a scale $s = 10$ kHz, and with an integration time $t_{\rm int} = 1000$ h. Lower panels: $\sigma_{\rm abs}/\sigma_{\rm obs}$ corresponding to the upper panels.

and n represents additive noise. The noise is given by the radiometer equation

$$\sigma_n = \frac{1}{n_{\rm s}} \frac{\rm SEFD}{\sqrt{N\,(N-1)\,t_{\rm int}\Delta\nu}}, \tag{3}$$

where $n_{\rm s}$ is the system efficiency, $\Delta\nu$ is the bandwidth, $t_{\rm int}$ is the integration time and N is the number of stations. We assume that $n_{\rm s} = 0.5$ and $N = 48$. The system equivalent density is given by

$${\rm SEFD} = \frac{2\kappa_{\rm B} T_{\rm sys}}{N_{\rm dip}\eta_\alpha A_{\rm eff}}, \tag{4}$$

where $\kappa_{\rm B}$ is Boltzmann's constant, $A_{\rm eff} = \min(\frac{\lambda^2}{3}, 1.5626)$ is the effective area of each dipole in the dense and sparse array regimes, respectively, $N_{\rm dip}$ is the number of dipoles per station (24 tiles times 16 dipoles per tile for a LOFAR core station) and η_α is the dipole efficiency which we assume to be 1. The system noise $T_{\rm sys}$ has two

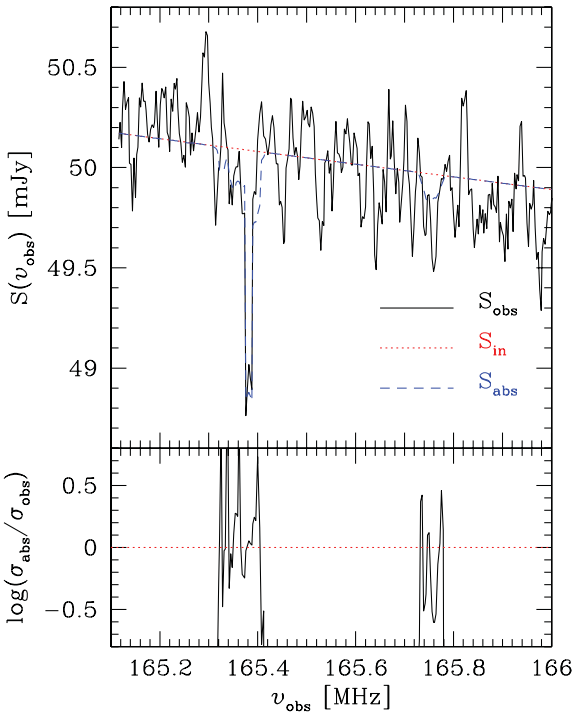

Figure 12. Upper panel: spectrum of a source positioned at $z = 7.6$ (i.e. $\nu \sim 165$ MHz), with an index of the power law $\alpha = 1.05$ and a flux density $S_{\rm in}(z_s) = 50$ mJy. The lines are the same as those in Fig. 10. Here we have assumed the noise σ_n given in equation (3), a bandwidth $\Delta\nu = 5$ kHz, smoothing over a scale $s = 5$ kHz and an integration time $t_{\rm int} = 1000$ h. The IGM absorption is calculated from the reference simulation $\mathcal{L}4.39$. Lower panel: $\sigma_{\rm abs}/\sigma_{\rm obs}$ corresponding to the upper panel. Note that this LOS has been chosen to intercept a strong absorption feature, with $\tau_{21\rm cm} = 0.12$.

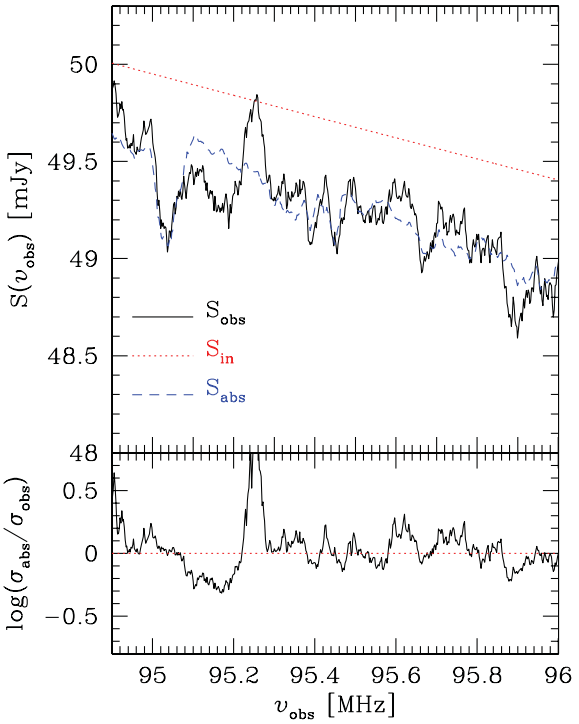

Figure 13. Upper panel: spectrum of a source positioned at $z = 14$ (i.e. $\nu \sim 95$ MHz), with an index of the power law $\alpha = 1.05$ and a flux density $S_{\rm in}(z_s) = 50$ mJy. The lines are the same as those in Fig. 10. Here we have assumed the noise σ_n given in equation (3), a bandwidth $\Delta\nu = 20$ kHz, smoothing over a scale $s = 20$ kHz and an integration time $t_{\rm int} = 1000$ h. The IGM absorption is calculated from the reference simulation $\mathcal{L}4.39$. Lower panel: $\sigma_{\rm abs}/\sigma_{\rm obs}$ corresponding to the upper panel.

contributions: (i) from the electronics and (ii) from the sky. We assume that the sky has a spectral index of -2.55, obtaining $T_{\rm sys} = [140 + 60(\nu/150\,{\rm MHz})^{-2.55}]$ K.

The complete Fourier plane sampling can be done by evaluating the above equation for every set of baseline coordinates. The predicted visibilities are then gridded and transformed via inverse Fourier transforms in order to obtain the dirty images.

For the purpose of the 21 cm forest, fine spectral resolution is needed, which means that the spectra need to be predicted for a large number of channels ($\sim$10 000). Thankfully, the computation can be done independently for each channel, and the maps can thus be evaluated in parallel. After assembling the full image cube, the LOS spectrum is extracted.

In the upper panels of Fig. 10 we show the spectrum of a source positioned at $z_s = 10$ (i.e. $\nu \sim 129$ MHz). The intrinsic radio source spectrum, $S_{\rm in}$, is assumed to be similar to Cygnus A (see also Carilli et al. 2002; Mack & Wyithe 2012), with a power-law index $\alpha = 1.05$ and a flux density $S_{\rm in}(z_s) = 50$ mJy. It should be noted that if the intrinsic radio spectrum were not a pure power law, the identification of absorption features would be rendered even more complex by the requirement that the continuum level must be fit as well. The simulated absorption spectrum, $S_{\rm abs}$, is calculated from the IGM optical depth found in our reference simulation $\mathcal{E}1.2$-$\alpha3$. The observed spectrum, $S_{\rm obs}$, is calculated assuming an observation time $t_{\rm int} = 1000$ h and a bandwidth $\Delta\nu = 20$ kHz. The spectra are plotted at the resolution of the simulation, unless stated otherwise. While some absorption features are evident, it is not obvious that we will be able to disentangle them from the instrumental noise.

Even though our simulation box reaches gas overdensities δ as high as a few tens, typically an LOS through the IGM samples mild overdensities $\delta \sim 1$. As an example, while $\sim$40 per cent of cells along the LOS in the figure (in the full redshift range $z = 6.5$–15) have $\tau_{21\rm cm} > 0.005$, none has $\tau_{21\rm cm} > 0.025$, setting a limit on the gas transmissivity of $e^{-\tau_{21\rm cm}} > 0.975$. Thus, similar to e.g. Mack & Wyithe (2012), we do not find narrow strong absorption lines (see below for further discussion). If we do a Gaussian smoothing of the spectrum over a scale $s = 10$ kHz (upper-middle panel) or reduce the noise by a factor of 0.1 (similar to what is expected from the SKA; upper-right panel), then the observability improves. This is more evident in the lower panels of the figure, which show the quantity $\sigma_{\rm abs}/\sigma_{\rm obs}$, where $\sigma_i = S_i - S_{\rm in}$ and $i =$ abs, obs.

Stronger absorption features appear if we use model $\mathcal{L}4.39$, in which larger overdensities are present (see Section 3.1). This is visible in Fig. 11, where $S_{\rm in}$, $S_{\rm abs}$ and $S_{\rm obs}$ are shown for the same source of Fig. 10. The frequency range plotted is smaller to allow a better visualization of the absorption features. In this case the prospect for a detection improves, even halving the observation time (or, equivalently, the bandwidth). The third (fourth) panel from the left shows the case for $\Delta\nu = 2.5$ kHz ($\Delta\nu = 10$ kHz) and a smoothing of the spectrum over the same scale. While retaining a high resolution might result in a null detection, observation features are clearly visible if a larger bandwidth and smoothing scale are used. We have verified that features are detected for $\Delta\nu \gtrsim 5$ kHz. Similar to model $\mathcal{E}1.2$-$\alpha3$, along an LOS in the same redshift range, here we have $\sim$40 per cent of cells with $\tau_{21\rm cm} > 0.005$, but we also find a handful of cells with $\tau_{21\rm cm} > 0.1$, corresponding to a gas transmissivity $e^{-\tau_{21\rm cm}} < 0.905$.

If we were lucky enough to intercept one of such high-density pockets of gas (with $\tau_{21\rm cm} > 0.1$; these cells are found in $\sim$0.1 per cent of the LOS), very strong absorption features could then be detected, as shown in Fig. 12, where we have located at $z = 7.6$ a radio source with the same characteristics as above. To calculate the observed spectrum we have now used a $\Delta\nu = 5$ kHz and an integration time $t_{\rm int} = 1000$ h. An even better prospect of detection would arise if e.g. a high-redshift damped Lyα system were intercepted, but the simulations employed in this work do not have the resolution to investigate this possibility, which will be addressed elsewhere.

Finally, moving towards higher redshift ($z > 12$), when most of the gas in the IGM is still neutral and relatively cold, would offer the chance of detecting a stronger average absorption. Although this range of redshift falls outside the one observed by LOFAR because of strong RFI contamination (Offringa et al. in preparation), it is still interesting to look at the example shown in Fig. 13, where the usual reference radio source has been located at $z = 14$. The figure clearly shows that a LOFAR-type telescope could easily detect the global absorption (rather than the single absorption features observed at lower redshift) due to the highly neutral IGM if a relatively large bandwidth is used. The figure also shows the results for $\Delta\nu = 20$ kHz, but a suppression of the source flux could also be detected for $\Delta\nu = 10$ kHz. It should be noted, however, that distinguishing a suppression of the source flux due to intervening neutral hydrogen from a source with an intrinsically lower flux would not be straightforward.

6 CONCLUSIONS

In this paper we have discussed the feasibility of the detection of the 21 cm forest in the diffuse IGM with the radio telescope LOFAR. The optical depth to the 21 cm line has been derived using the simulations of reionization presented in C2012, which reproduce a number of observational constraints such as the Thomson scattering optical depth (Komatsu et al. 2011) and the H I photoionization rate at $z \sim 6$ (Wyithe & Bolton 2011; Calverley et al. 2011). The simulations provide the evolution of the spatial distribution of relevant physical properties such as gas neutral fraction, temperature and velocity field. The main results of our investigation can be summarized as follows.

(i) The spectra from reionization models with similar total comoving hydrogen ionizing emissivities, but different frequency distributions, look remarkably similar. Thus, unless the reionization histories are very different from each other (e.g. a predominance of UV versus X-ray heating), we do not expect to distinguish them by means of observations of the 21 cm forest.

(ii) The photo-heating associated with the presence of a strong X-ray background would make the detection of the 21 cm line absorption impossible. The lack of absorption could then be used as a probe of the presence/intensity of the X-ray background and the thermal history of the Universe.

(iii) Along a random LOS, LOFAR could detect a global suppression of the spectrum from $z \gtrsim 12$, when the IGM is still mostly neutral and cold, in contrast with the more well-defined, albeit broad, absorption features visible at lower redshift. Sharp, strong absorption features associated with rare, high-density pockets of gas could be detected at $z \sim 7$ along preferential lines of sight.

The most challenging aspect of the detection of a 21 cm forest remains the existence of high-z radio loud sources. Although a Quasi Stellar Object has been detected at $z = 7.085$ (Mortlock et al. 2011), the existence of even higher redshift quasars is uncertain. The predicted number of radio sources which can be used for 21 cm forest studies in the whole sky per unit redshift at $z = 10$ varies in the range $10-10^4$ depending on the model adopted for the luminosity function of such sources and the instrumental characteristics (e.g. Carilli et al. 2002; Xu et al. 2009), making such a detection an extremely challenging task. The possibility of using Gamma Ray Burst afterglows has been suggested by Ioka & Mészáros (2005), concluding that it will be difficult to observe an absorption line, even with the SKA, except for very energetic sources, such as GRBs from the first stars. In fact, a similar calculation has been repeated more recently by Toma, Sakamoto & Meszaros (2011) for massive metal-free stars, finding that the flux at the same frequencies should typically be at least an order of magnitude higher than for a standard GRB.

An absorption feature stronger than the one produced by the diffuse IGM would be the one due to intervening starless minihaloes or dwarf galaxies (i.e. Meiksin 2011; Xu et al. 2011), resulting in an easier detection. On the other hand, the optical depth would strongly depend on the feedback effects acting on such objects. Because of the large uncertainties about the nature and intensity of high-z feedback effects (for a review see Ciardi & Ferrara 2005 and its arXiv updated version), it is not straightforward to estimate the relative importance of these two absorption components unless a self-consistent calculation is performed. We defer this investigation to a future paper.

ACKNOWLEDGMENTS

The authors would like to thank an anonymous referee for his/her comments. This work was supported by DFG Priority Programs 1177 and 1573. GH is a member of the LUNAR consortium, which is funded by the NASA Lunar Science Institute (via Cooperative Agreement NNA09DB30A) to investigate concepts for astrophysical observatories on the Moon. LVEK, HV and SD acknowledge the financial support from the European Research Council under ERC-Starting Grant FIRSTLIGHT 258942.

REFERENCES

Baek S., Di Matteo P., Semelin B., Combes F., Revaz Y., 2009, A&A, 495, 389
Bernardi G. et al., 2009, A&A, 500, 965
Bernardi G. et al., 2010, A&A, 522, A67
Bowman J. D., Morales M. F., Hewitt J. N., 2009, ApJ, 695, 183
Calverley A. P., Becker G. D., Haehnelt M. G., Bolton J. S., 2011, MNRAS, 412, 2543
Carilli C. L., Gnedin N. Y., Owen F., 2002, ApJ, 577, 22
Carilli C. L., Wang R., van Hoven M. B., Dwarakanath K., Chengalur J. N., Wyithe S., 2007, AJ, 133, 2841
Ciardi B., Ferrara A., 2005, Space Sci. Rev., 116, 625
Ciardi B., Madau P., 2003, ApJ, 596, 1
Ciardi B., Ferrara A., Marri S., Raimondo G., 2001, MNRAS, 324, 381
Ciardi B., Salvaterra R., Di Matteo T., 2010, MNRAS, 401, 2635
Ciardi B., Bolton J. S., Maselli A., Graziani L., 2012, MNRAS, 423, 558
Datta K. K., Majumdar S., Bharadwaj S., Choudhury T. R., 2008, MNRAS, 391, 1900
Di Matteo T., Perna R., Abel T., Rees M. J., 2002, ApJ, 564, 576
Di Matteo T., Ciardi B., Miniati F., 2004, MNRAS, 355, 1053
Dijkstra M., Gilfanov M., Loeb A., Sunyaev R., 2012, MNRAS, 421, 213
Furlanetto S. R., 2006, MNRAS, 370, 1867
Furlanetto S. R., Loeb A., 2002, ApJ, 579, 1
Furlanetto S. R., Oh S. P., Briggs F. H., 2006, Phys. Rep., 433, 181
Geil P. M., Wyithe J. S. B., 2009, MNRAS, 399, 1877

Geil P. M., Wyithe S., Petrovic N., Oh P., 2008, MNRAS, 390, 1496
Gleser L., Nusser A., Benson A. J., 2008, MNRAS, 391, 383
Ioka K., Mészáros P., 2005, ApJ, 619, 684
Jelić V. et al., 2008, MNRAS, 389, 1319
Komatsu E. et al., 2011, ApJS, 192, 18
Lidz A., Zahn O., McQuinn M., Zaldarriaga M., Hernquist L., 2008, ApJ, 680, 962
Liu A., Tegmark M., Bowman J., Hewitt J., Zaldarriaga M., 2009, MNRAS, 398, 401
Mack K. J., Wyithe J. S. B., 2012, MNRAS, 425, 2988
Madau P., Meiksin A., Rees M. J., 1997, ApJ, 475, 429
Maselli A., Ferrara A., Ciardi B., 2003, MNRAS, 345, 379
Maselli A., Ciardi B., Kanekar A., 2009, MNRAS, 393, 171
Meiksin A. A., 2009, Rev. Mod. Phys., 81, 1405
Meiksin A., 2011, MNRAS, 417, 1480
Mellema G., Iliev I. T., Pen U., Shapiro P. R., 2006, MNRAS, 372, 679
Morales M. F., Wyithe J. S. B., 2010, ARA&A, 48, 127
Mortlock D. J. et al., 2011, Nat, 474, 616
Partl A. M., Maselli A., Ciardi B., Ferrara A., Müller V., 2011, MNRAS, 414, 428
Pelupessy F. I., Di Matteo T., Ciardi B., 2007, ApJ, 665, 107
Pierleoni M., Maselli A., Ciardi B., 2009, MNRAS, 393, 872
Santos M. G., Amblard A., Pritchard J., Trac H., Cen R., Cooray A., 2008, ApJ, 689, 1
Santos M. G., Ferramacho L., Silva M. B., Amblard A., Cooray A., 2010, MNRAS, 406, 2421
Shaver P. A., Windhorst R. A., Madau P., de Bruyn A. G., 1999, A&A, 345, 380
Springel V., 2005, MNRAS, 364, 1105
Toma K., Sakamoto T., Meszaros P., 2011, ApJ, 731, 127
Tozzi P., Madau P., Meiksin A., Rees M. J., 2000, ApJ, 528, 597
Wyithe J. S. B., Bolton J. S., 2011, MNRAS, 412, 1926
Xu Y., Chen X., Fan Z., Trac H., Cen R., 2009, ApJ, 704, 1396
Xu Y., Ferrara A., Chen X., 2011, MNRAS, 410, 2025

This paper has been typeset from a TEX/LATEX file prepared by the author.